Investigation of periodically driven systems by x-ray absorption spectroscopy using asynchronous data collection mode

H. Singh, D. Donetsky, J. Liu, K. Attenkofer, B. Cheng, J. R. Trelewicz, I. Lubomirsky, E. Stavitski, and A. I. Frenkel

Citation: Review of Scientific Instruments **89**, 045111 (2018); doi: 10.1063/1.5000679
View online: https://doi.org/10.1063/1.5000679
View Table of Contents: http://aip.scitation.org/toc/rsi/89/4
Published by the American Institute of Physics

Investigation of periodically driven systems by x-ray absorption spectroscopy using asynchronous data collection mode

H. Singh,[1] D. Donetsky,[2] J. Liu,[2] K. Attenkofer,[3] B. Cheng,[1] J. R. Trelewicz,[1,4]
I. Lubomirsky,[5,a)] E. Stavitski,[3,a)] and A. I. Frenkel[1,a)]
[1]*Department of Materials Science and Chemical Engineering, Stony Brook University, Stony Brook, New York 11794, USA*
[2]*Department of Electrical and Computer Engineering, Stony Brook University, Stony Brook, New York 11794, USA*
[3]*National Synchrotron Light Source II, Brookhaven National Laboratory, Upton, New York 11973, USA*
[4]*Institute for Advanced Computational Science, Stony Brook University, Stony Brook, New York 11794, USA*
[5]*Department of Materials and Interfaces, Weizmann Institute of Science, Rehovot 76100, Israel*

(Received 17 August 2017; accepted 24 March 2018; published online 18 April 2018)

We report the development, testing, and demonstration of a setup for modulation excitation spectroscopy experiments at the Inner Shell Spectroscopy beamline of National Synchrotron Light Source - II. A computer algorithm and dedicated software were developed for asynchronous data processing and analysis. We demonstrate the reconstruction of X-ray absorption spectra for different time points within the modulation pulse using a model system. This setup and the software are intended for a broad range of functional materials which exhibit structural and/or electronic responses to the external stimulation, such as catalysts, energy and battery materials, and electromechanical devices. *Published by AIP Publishing.* https://doi.org/10.1063/1.5000679

I. INTRODUCTION

Design and discovery of new functional materials with improved performances and greater versatility are the key drivers of innovation. Such advanced nanoscale materials as catalysts and electrocatalysts,[1,2] electromechanical actuators,[3,4] battery and filtration materials[5,6] exhibit their new functionalities due to the changes in their local structures and electronic properties that occur within a range of a few interatomic distances.[1,7] There is a paucity of either available experimental methods or a dedicated research infrastructure in the case of materials in which the response to the external stimulation is weak. In the first class of such materials, such as piezoelectrics, ferroelectrics, classical electrostrictors, and magnetostrictors,[3,8,9] the structural or electronic responses to the external excitation are uniform but weak. In the second class, only a small subset of species in the material responds to the external stimulation. For instance, in a recently discovered non-classical electrostrictors only ca. 10% of Ce ions located near O ion vacancies provide a response to the modulations of the external electric field.[3,10] In this and the other materials, atomic-level characterization with sufficient sensitivity to probe a small fraction of affected host or dopant cations is critical for uncovering the nature of large electrostriction and other effects. Hence, the challenge is how to measure these changes that can be either small or heterogeneous in nature or both. This subject is in the focus of intense research, aimed at understanding the origins of emerging physicochemical properties and novel functionalities in such materials.[1,2,7] In this paper, we report on the development of a dedicated instrument at the National Synchrotron Light Source-II (NSLS-II) that enables such enhanced sensitivity by using the asynchronous excitation-probe mode of X-ray absorption fine-structure (XAFS) spectroscopy.

XAFS spectroscopy, which comprises X-ray Absorption Near-Edge Structure (XANES) and Extended X-ray Absorption Fine Structure (EXAFS), is a premier synchrotron-based technique, which delivers element-specific information on the chemical state and coordination environment around particular atomic species in a compound.[11] In EXAFS, the oscillatory structure of the absorption coefficient within 40-1000 eV past the absorption edge is caused by the interference of the outgoing and scattered photoelectron waves and is commonly described by the equation (within the ith shell)[11]

$$\chi(k) = \sum_i \frac{n_i S_0^2}{kR_i^2} \left| f_i^{eff}(k) \right| \sin\left[2kR_i + \delta_i(k)\right] e^{-2\sigma_i^2 k^2} e^{-\frac{2R_i}{\lambda_i(k)}}, \quad (1)$$

where k is the photoelectron wavenumber, $f_i^{eff}(k)$ and $\delta_i(k)$ are the photoelectron scattering-path amplitude and phase, respectively, S_0^2 is the passive electron-reduction factor, n_i is the degeneracy of the scattering path, R_i is the effective half-path length (which equals the interatomic distance for single-scattering paths), σ_i^2 is the mean-square deviation in R_i, and $\lambda_i(k)$ is the photoelectron mean free path.

As in any resonant technique, XAFS spectra are contributed by all X-ray absorbing atoms in the sample, and, hence, those Ce atoms (from the latter example of doped ceria) that do not contribute to electrostriction—the spectator ones—will dominate the XAFS spectrum and, hence, hinder the contribution of the electromechanically active Ce atoms. In the former systems with uniform but weak response to external perturbation, the spectral changes are often small and are difficult to analyze. In such cases, an attractive solution to

a)Authors to whom correspondence should be addressed: Igor.lubomirsky@weizmann.ac.il; istavitski@bnl.gov; and anatoly.frenkel@stonybrook.edu

increase the signal to noise ratio and better isolate the response of active species is a method of data collection where a periodic perturbation is introduced by an electric[3,8,10] or magnetic field,[9,12] or reacting gas composition.[13,14] As another example, we mention Modulated Excitation Spectroscopy (MES) technique,[15,16] combined with time-resolved XAFS.[17] In one widely used implementation of MES, the phase sensitive detection (PSD) procedure is used for obtaining the demodulated spectral intensity I as a function of the phase delay between the driving signal and the response,

$$I_k^{\varphi_k^{PSD}}(E) = \frac{2}{T}\int_0^T I(E,t)\sin(k\omega t + \varphi_k^{PSD})dt, \qquad (2)$$

where I (E, t) is the original signal (e.g., the XAFS spectrum) as a function of energy E and time t, ω is the external stimulation frequency, φ_k^{PSD}, $T = 2\pi/\omega$ are the demodulation phase angle and the modulation period, respectively, and $k = 1$ is the fundamental harmonic. By calculating the demodulated spectrum, $I(E)$ for phase angles between 0 and 2π, the spectra are transformed from the time domain into a phase domain. This procedure cancels out all parts of the measured spectra that do not follow the excitation frequency ω, which include the spectator species and noise, and hence MES contains only the signal of the changes imposed by the external stimulus. In this procedure, effectively, the demodulated spectra are obtained for each time point within a representative pulse, and the phase lag (retardation) between the excitation and response describes the time dependence of the spectra within the pulse.[17–19] The phase lag can thus be used to provide insight into kinetics and reaction mechanisms. Thus, the modulated excitation approach, wherein periodic perturbation of an external parameter is employed to stimulate the system under observation, while time-resolved data are collected simultaneously, can be applied for a system that responds reversibly to the external periodic excitation. These methods with periodic perturbation have been adopted by several groups including Ferri *et al.*,[13,18–21] Newton *et al.*,[1,22] and Pascarelli *et al.*,[9,12] at European Synchrotron Radiation Facility (ESRF) and Swiss Light Source (SLS), wherein mostly lock-in methods have been applied for measurements under *in situ* or *operando* conditions. These studies showed the potential of MES for XAFS as it drastically increased sensitivity to weak response of the systems under external stimulation. Frenkel and Lubomirsky *et al.* have also applied the pulsed perturbation (via electric field) while collecting time-resolved XAFS data in the doped CeO_2, to discover the origin of enormous electrostriction in Gd doped CeO_2.[3,10,23,24]

We report on the new versatile setup that enables the asynchronous data collection and processing using experiments with periodic stimulations. This capability, implemented at the Inner Shell Spectroscopy (ISS) beamline of NSLS-II, is intended for studies of a variety of materials under modulated conditions, wherein materials exhibit dynamic response to external perturbation, such as electric, magnetic, temperature, pressure, gas composition, and electromagnetic radiation (e.g., UV or visible light).[1,7,9,25] In addition to the versatility of our setup, the data sorting algorithm used in post-processing of the time-dependent spectra is an alternative to a commonly used lock-in method, limited to the use with photon counting electronics providing analog signals. As we explain in greater detail below, pulsed experiments in which the time duration of X-ray scans and excitation pulse periods are fixed will suffer from non-uniform density of energy points within effective time intervals. That will limit both time resolution and spectral density of the X-ray absorption spectra. When the X-ray scans and excitation pulses are asynchronous, the energy points will be spread more uniformly over the time intervals. We have thus implemented the "asynchronous" mode of data acquisition. In our approach, we reconstruct the spectra for a number of time points within a stimulation period from a sequence of absorption coefficient data collected asynchronously over the large number of periods of external stimulation of the sample,

$$\{\mu_i(t)\}_{i=1}^{N} \rightarrow \left\{\mu_j(E)\right\}_{j=1}^{M}. \qquad (3)$$

The left-hand side of Eq. (3) contains N values of the absorption coefficient collected over many periods of external stimulation. If one sorts these values as a function of the X-ray energy, they cannot be simply interpreted without additional processing because any adjacent values $\mu(E_i)$ and $\mu(E_{i+1})$ correspond to different states of the sample. The data therefore should be binned into M time intervals so that each time bin t_j within an oscillation period corresponded to the entire spectrum $\mu_j(E)$, shown in the right-hand side of Eq. (3). Figure 1 shows the time dependence of the monochromator trajectory, the square-wave signal used for modulation and data sorting, assignment of bin numbers within a constant voltage level, and examples of reconstructed spectra corresponding to different time bins. After such sorting, the $\mu(E, t)$ data will be available for analysis by the phase sensitive detection methods as well as various types of difference methods (e.g., Δ-XANES[1,10,26]).

We note that if the time duration of X-ray energy scan T_E is a multiple of the pulse periods T_P of an external simulation (a synchronous data collection mode), that is, $T_E = mT_P$, where m is an integer, some bins in the representative pulse [Fig. 1(e)] will be oversampled, some—empty. Even in a more general case of $nT_E = mT_P$, where n, m are integers, after n energy scans elapsed, no improvement in time resolution can be expected. We have enabled the asynchronous modulation excitation-probe technique, where the time durations of the energy scan and external stimulation period are not synchronized, allowing us to improve the time resolution and spectral density of the spectra. In our setup, we used wave function generator for providing periodic modulation. The synchronizing signal is recorded by the beamline data acquisition system in the same file where the X-ray absorption data are stored. Both the waveform generator signal and the monochromator energy values are referenced to the same Global Positioning System (GPS) time that is recorded in the data file. To test the setup and sorting algorithm, we simulated external perturbation by using a mechanical actuator that periodically switched between the two samples containing the same element. Thus, during the first half of the square wave period T_P, one sample was probed by XAFS, and during the second half—the other sample. Due to the large differences in the nature of two samples, the changes in their absorption coefficients were supposed to simulate the effects of periodic excitation in future applications of our approach.

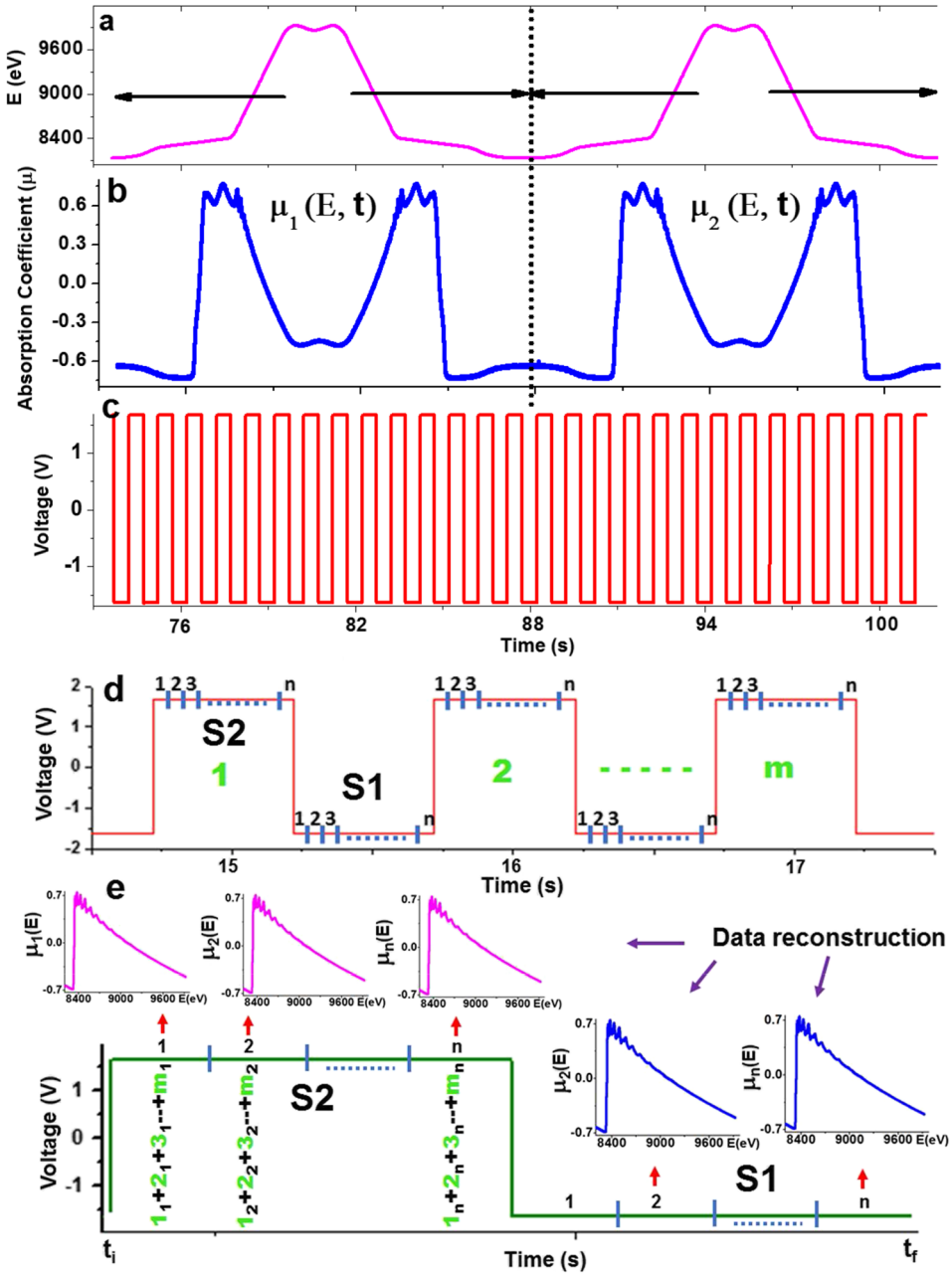

FIG. 1. Schematic of an asynchronous detection mode showing a prototype time dependent XAFS data collection and their reconstruction. (a) Synchrotron energy profile as a function of time scanned near the Ni K-edge. (b) The corresponding absorption coefficient as a function of time, showing two representative scans μ_1 and μ_2. (c) The square wave of 1 Hz period was used to switch between the samples S1 and S2 (each sample was exposed to the beam for 0.5 s). (d) The enlarged pulses are shown to demonstrate the procedure of dividing the pulses in the same number (n) of intervals or bins. (e) Illustration of the data reconstruction procedure, where m_n means n-th bin in the m-th pulse.

The spectra corresponding to each time bin within a pulse were reconstructed from the experimental time-energy scans and then processed in MatLab. In this Article, we characterize and demonstrate the reliability of this method and evaluate the effects of the experimental parameters on the signal to noise ratio, the time resolution, and the spectral density in the data.

II. EXPERIMENTAL

A. Sample details

For this work, we investigated 6 μm-thick films of $Ni_{0.75}W_{0.25}$. Two different samples were annealed at different temperatures and hence were of two different average grain sizes (see Table I for more details). We have designated these two samples as S1 and S2. The importance of their selection for this demonstration experiment is that they are good samples for the transmission mode and show good contrast in their XANES and EXAFS spectra.

B. Setup at the ISS beamline

ISS is the hard X-ray (4–36 keV) spectroscopy beamline at NSLS-II, designed to deliver 2×10^{14} ph/s in the monochromatic beam at full accelerator current and dedicated to *in situ*

TABLE I. Experimental details on the Ni-W samples.

Sample (NiW)	Heat treatment (°C) for 24 h	Grain size (nm)
S1	150	5
S2	600	60

and *operando* research. It uses a cryogenically cooled double crystal monochromator (DCM) designed to manage the heat load of the damping wiggler insertion device.[27,28] The DCM is driven by a direct drive servo motor, which allows it to perform XAFS scans in the continuous (slew scan) mode. The speed, combined with the *operando* infrastructure fully integrated with the control system, makes the beamline uniquely suited for sensitive XAFS experiments. One of the experimental end stations of ISS is equipped with ion chambers for transmission experiments, as well as Passivated Implanted Planar Silicon (PIPS) and Silicon Drift Detector (SDD) detectors for fluorescence measurements.

The data collection at ISS is performed using custom Field Programmable Gate Array (FPGA)-based Data Acquisition (DAQ) boards, developed to collect incremental encoder and analog data to acquire the monochromator position and detector currents, respectively. These devices receive the GPS time record and are capable to timestamp the signals with 8 ns resolution.[29] The data from each signal channel are stored on a hard drive via the EPICS interface. During post-processing, the timestamp is used to cross-correlate the signals from different channels to produce an XAS spectrum. In addition, the DAQ board can capture and timestamp digital signals as well as produce TTL outputs. This feature was used to apply periodic stimulation to the sample through a waveform generator (Agilent 33220A) that was supplying a pulsed signal to operate the mechanical actuator. The actuator is designed to operate up to a voltage of 10 V and a current of 200 mA. The two samples, S1 and S2, were positioned side by side on a sample holder, separated by 5 mm distance. During the data collection, the actuator was moving the samples to position either sample S1 or S2 into the beam path. The XAFS experiment has been performed in the transmission mode at the Ni K-edge (8.333 keV). The measurements were performed in two ways. First, we collected the data in the static mode, to obtain reference spectra for comparing with the reconstructed spectra after the post-processing of the data obtained in the pulsed mode. In this latter mode, we continuously switched the samples and the voltage output (denoted here as "high" or "low" levels for each state of the actuator) of the waveform generator was recorded. The samples were switched with 1 Hz frequency, and XAFS data were collected for ca. 60 min with a scan duration time of ca. 10–25 s. Due to a small drift in the energy scan time (of the order of 0.3-0.5 s), the energy scans were not in a constant temporal relationship with the actuator cycles, a necessary condition for the asynchronous data collection mode.

Figures 2(a) and 2(b) show the sampling rate f, per eV, in the energy interval ΔE (here: 2 eV) for samples S1 and S2 measured during one representative monochromator scan in the forward direction. The reason for the order of magnitude change in the sampling rates in different energy regions is due to the different significance of several regions in a typical X-ray absorption spectrum. Indeed, in the pre-edge, where the X-ray absorption coefficient changes monotonically, the faster sampling rate is used [Fig. 2(c)] compared to the XANES region, where the X-ray absorption coefficient changes rapidly to provide greater spectral density. Furthermore, in the EXAFS range, the sampling rate increases again

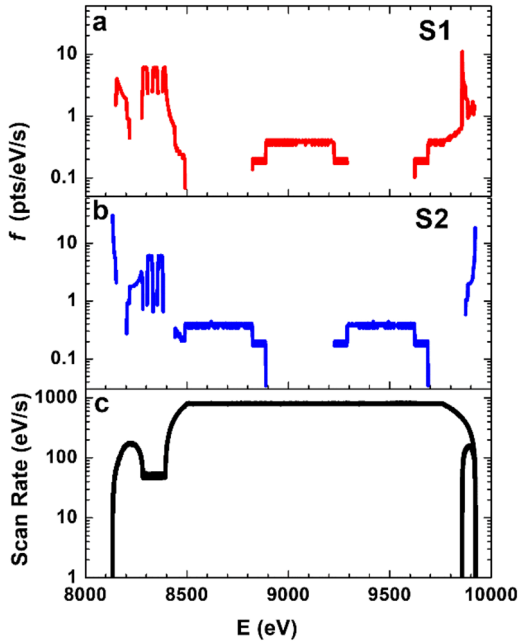

FIG. 2. The sampling rate f per sample (a) S1 or (b) S2 measured during one monochromator scan (in the forward direction). The scan rate (c) varied from ca. 50 eV/s in the XANES region of the spectrum to ca. 800 eV/s in the EXAFS region.

and the spectral density decreases [Fig. 2(c)]. Representative data shown in Fig. 2 are available to the users and can be used for optimizing the monochromator trajectory (e.g., for improving the spectral density and time resolution and also signal to noise ratio). We note also that the existence of multiple sampling rates is advantageous for asynchronous data collection purpose.

C. Data sorting algorithm

The main steps of the sorting algorithm are presented here. Since we applied it to the data obtained by mechanically switching two samples, S1 and S2, we will continue using this notation. In the context of a real experiment with modulated stimulation, the names S1 and S2 indicate two different states of the same sample during the positive and negative parts of a wave period. At the first step, we used the voltage values of the square wave pulse at the output of the waveform generator to separate the data corresponding to the samples S1 and S2. In the rest of the algorithm, the pulse width was divided in equal intervals (bins) and the data for each energy value and time were placed in the corresponding time bin within the pulse. When the process finished, each time bin contained a collection of the absorption coefficient values at different energies (see Fig. 1), allowing us to combine them in a spectrum. For reconstructing the XAFS spectra within a representative pulse, we divided each half (corresponding to either sample S1 or S2) of the m pulses by n intervals or bins [Fig. 1(d)]. The XAFS spectrum $\mu_j(E)$ corresponding to a certain bin j within a representative pulse [see Eq. (1)] was then constructed by combining all $\{E(t_i), \mu(t_i)\}$ values collected over the entire duration of the experiment. In this procedure, only those values of t_i that were located within the bins j in all pulses were selected for constructing $\mu_j(E)$ for each sample.

III. RESULTS AND DISCUSSION

A. Data reconstruction and processing

To validate the sorting algorithm and the software program that implemented it, we compared the reconstructed data with the data obtained in the static (conventional) mode for both the samples (Fig. 3). This figure shows the XAFS spectra of S1 and S2 in energy E(a, b), wavenumber k(c), and distance R(d) spaces. We show the reconstructed experimental raw data in energy space in addition to their difference spectra (the difference has been plotted by subtracting the static data from the reconstructed data). We have applied smoothing to the XAFS data due to the very large number of experimental data points in the measured data. After comparing the two types of data smoothing (linear and Gaussian), the linear method was found to be in better agreement with the static data. One can see that the reconstructed and static XAFS data are in good agreement.

B. Parameter optimization

In this section, we characterize the applicability of this method in terms of the effects of experimental conditions on the signal to noise ratio and the density of the reconstructed spectra. These effects were studied as a function of number of bins (from 1 to 500) that we used to divide the half-pulse width.

1. Signal to noise ratio

To analyze the signal to noise ratio (S/N) in the reconstructed spectra as a function of the number of bins, we follow the procedure of Dent *et al.*[30] which is described as follows. (i) Select few points around a datum in the spectrum; (ii) fit a low order–polynomial (we used the third order); (iii) for the data point in the middle of the selection assign the root mean square (rms) deviation of all these points relative to the polynomial as the noise; and (iv) repeat this process for all points in the spectrum. To calculate the "signal," we analyzed the absorption coefficient data above the absorption edge with respect to the trend line that is used for the edge step normalization. Each oscillation maximum or minimum value, divided by the edge step $\Delta\mu z$, where z is the sample thickness, was defined as a "signal." For each "signal" value, we have defined σ as follows: $\sigma^2 = \left\langle (x_i - \bar{x})^2 \right\rangle$, where $\bar{x}$ is the mean and the angular brackets denote the averaging over all data points in 2 eV interval centered around the corresponding maximum or minimum. After that the "noise" value was obtained by dividing σ by the edge step. This procedure is illustrated for sample S1 in Fig. 4, showing the post-edge oscillations of the absorption

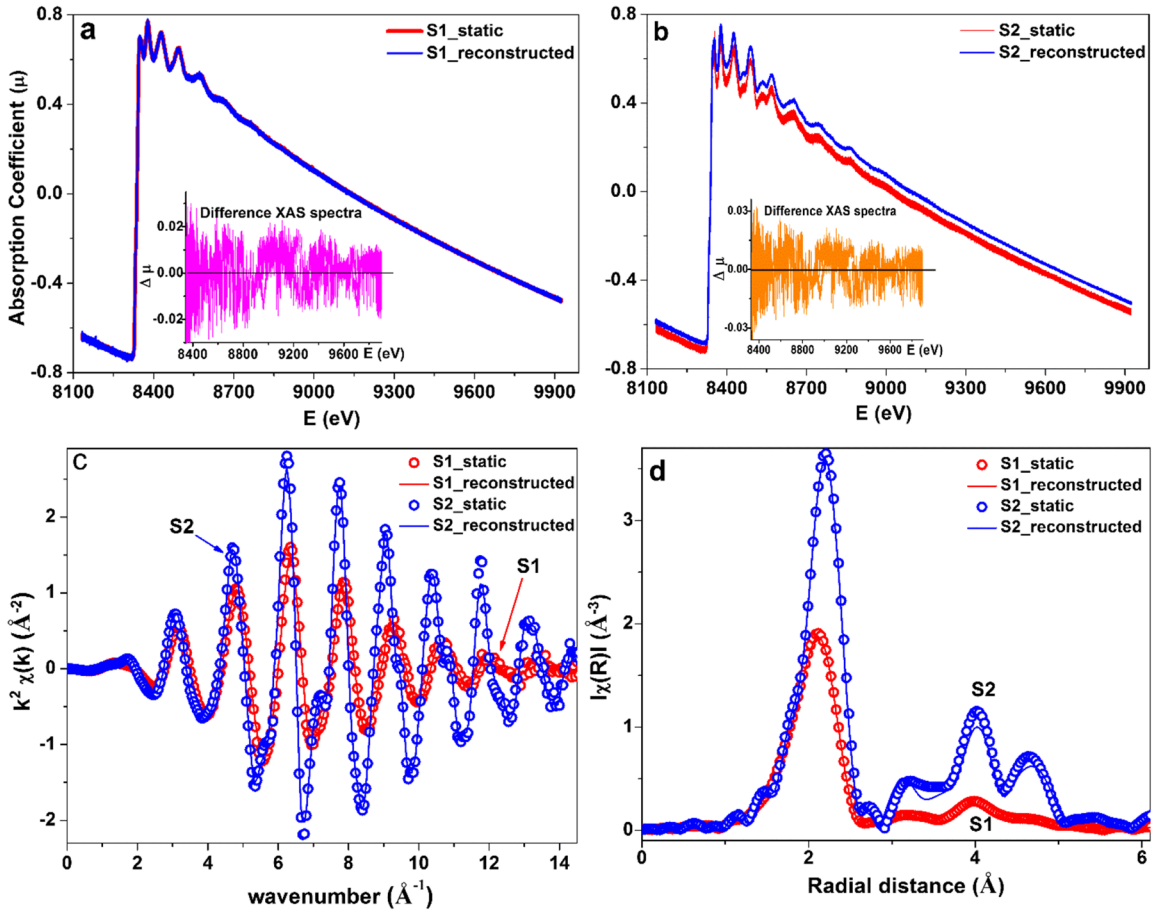

FIG. 3. Ni K-edge raw static and reconstructed XAFS spectra of S1 (a) and S2 (b). Insets represent the residual spectra of S1 (a) and S2 7(b), obtained by subtracting the static data from the reconstructed ones. The k^2-weighted and "smoothed" XAFS spectra of both the reconstructed and static S1 and S2 samples are shown in k space (c) and R space (d). Fourier transform was carried out in the k range from 2.0 Å^{-1} up to 14.0 Å^{-1}.

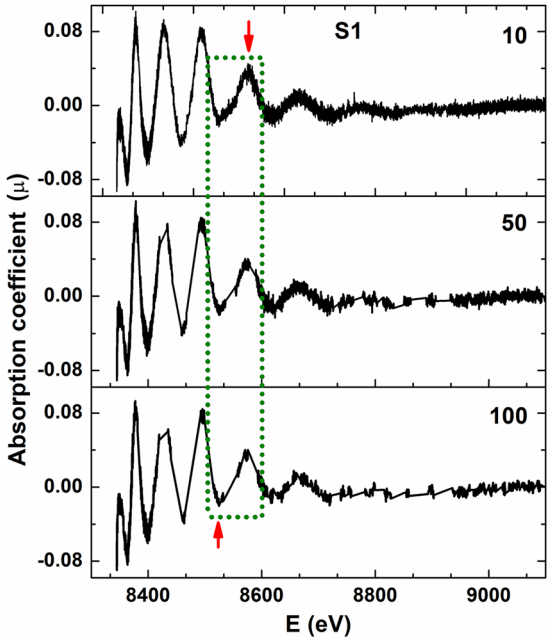

FIG. 4. Demonstration of the signal to noise calculation procedure (shown for sample S1). Three curves correspond to the 5th, 25th, and 50th bins, when a total of 10, 50, or 100 bins (marked next to each curve), respectively, were used to divide the half-pulse. The rectangular region highlights the data used in evaluating the noise and the S/N ratio presented in Table II near the local minimum and the maximum of the curves, shown by arrows.

coefficient (after subtracting the trend line) and two points chosen for the S/N evaluation. Three curves were chosen in Fig. 4, calculated for the central bins for the total numbers of 10, 50, and 100 bins. As evident in Fig. 4 and Table II, the noise decreases and the S/N ratio increases when the total number of bins increases. To understand this trend, the detailed analysis of the noise spectrum is needed, which is beyond the scope of this work.

2. Spectral density

To investigate the second important experimental factor—spectral density—as a function of number of time bins (10, 100, and 500), we have analyzed the quality of all the reconstructed XAFS data in terms of the selected number of bins. As expected, the higher spectral density is obtained for smaller number of bins due to the larger number of data points (Fig. 5). This plot shows the loss of spectral density on increasing the number of time bins. For the smallest number of time bins (e.g., 10), the spectral density is similar to that of the static XAFS data. In order to optimize the data processing parameters, such as the number of time bins to be used in the reconstruction, it is therefore important to rely on both S/N and spectral density behaviors.

TABLE II. Absolute values of the signal-to-noise values for three spectra obtained within central bins for 10, 50, and 100 bin numbers for the two representative energies, E_1 and E_2, shown by arrows in Fig. 4.

	E_1 = 8524 eV		E_2 = 8575 eV	
Number of time bins	S/N	Noise (σ)	S/N	Noise (σ)
10	4.9	2.2×10^{-3}	8.2	2.7×10^{-3}
50	6.5	2.5×10^{-3}	14	1.6×10^{-3}
100	17	6.6×10^{-4}	38	5.8×10^{-4}

3. Dependence on the number of time bins

Finally, to analyze the time dependence of the data within a selected number of time bins, we have chosen the n = 50, 100, and 500 bins and examined the absorption spectra as a function of time within the half pulse for each sample, that is, as a function of the time bin number within each half pulse. To investigate the sensitivity of the data to the different number of time bins, we plotted representative XAFS spectra of both samples S1 and S2 for n = 100 (Fig. 6). The data show that in the earlier times for each sample the spectra differ from the remainder of the half pulse.

For a more accurate view of such experimental time dependence deviation, we have plotted the standard deviation of these reconstructed spectra from the static spectra as a function of time (bin number) within a representative pulse divided by n = 100 bins for both samples S1 and S2. For this, we have chosen the energy range between 8362 eV and 8365 eV which shows minimum deviation of the data points from the mean value of each interval. Figure 7 shows the standard deviation of reconstructed data relative to the static data as a function of time for samples S1 and S2. Coincidentally, this behavior resembles the relaxation behavior of several materials including dielectrics which decay exponentially with time in response to the applied electric field.[31,32]

In our case, the samples were not modified during the measurements and thus neither their physical state nor the corresponding XAFS spectra were expected to show relaxation behavior. An explanation of these deviations of XAFS spectra of both samples during the initial time bins from the rest of the pulse interval is illustrated in Fig. 8. It shows the measured raw XAFS spectra as a function of time and applied voltage (that varied between +1.67 V and −1.63 V). As discussed earlier, each state of the voltage is associated with one or the other sample (in our case, the value of +1.67 V is associated with S1 and −1.63 V is associated with S2). A close observation of the sample's XAFS spectrum shows a time lag between the voltage switching time and the sharp spike corresponding to the moment where the X-ray beam was transmitted through a thin piece of plastic material separating the two samples. That delay is explained by an inductance effect of the mechanical actuator, and its result is the contamination of the spectrum assigned to the sample S1 in the beginning of the pulse by the spectrum coming from the sample S2 and vice versa. The fortunate effect for the purpose of this investigation is that these data imitated the relaxation effects in "real" modulated experiments, where in the beginning of the pulse the spectra may exhibit differences from those corresponding to the later time.

4. Dependence on the time interval for data reconstruction

In this section, we evaluate the minimum required time for the adequate data reconstruction so that the experimenter

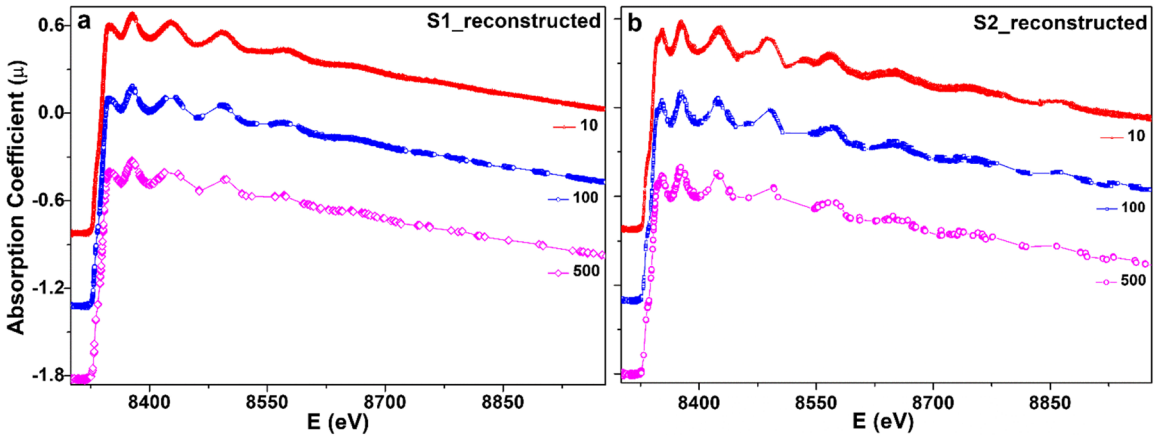

FIG. 5. Reconstructed XAS data for three different numbers of time bins used in the reconstruction: 10, 100, and 500, for samples S1 (a) and S2 (b). In all cases, the reconstruction was done for the central bin in the half pulse.

could decide on the duration of the total measurement time in planning the experiment. We performed the data reconstruction as a function of measurement time using the first 100 s, 300 s, 500 s, 700 s, 1000 s, and 2000 s from the beginning of the experiment. In order to obtain the best case scenario, we used a single bin, i.e., the entire pulse, duration, for the data reconstruction. Our analysis indicates that the 100 s of measurement time was sufficient for data reconstruction, as validated by comparison with the static data [Fig. 9(a) shows such representative reconstruction for sample S2]. When three time bins were used, our analysis shows that for the central time bin 700 s is sufficient for the data reconstruction [Fig. 9(b), showing such representative reconstruction for sample S1]. These results are, of course, specific to the particular sampling scan

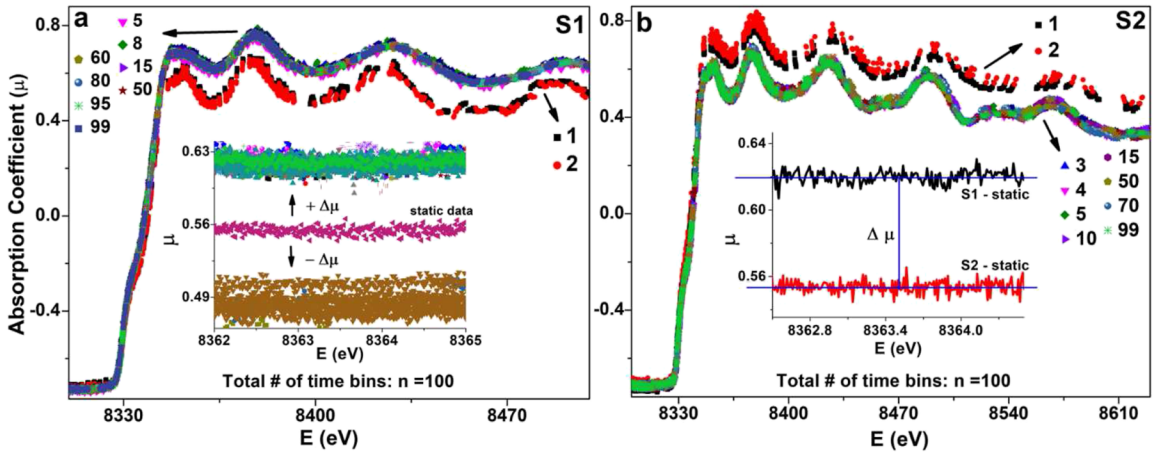

FIG. 6. Representative XAFS spectra of both samples S1 (a) and S2 (b) as a function of time within the pulse (defined here by the time bin number 1, 2, . . ., 99) for a given total number (100) of time bins. Insets show the typical variations of the reconstructed XAFS spectra from the static signal [(a) inset] and the typical difference between the two static XAFS signals [(b) inset].

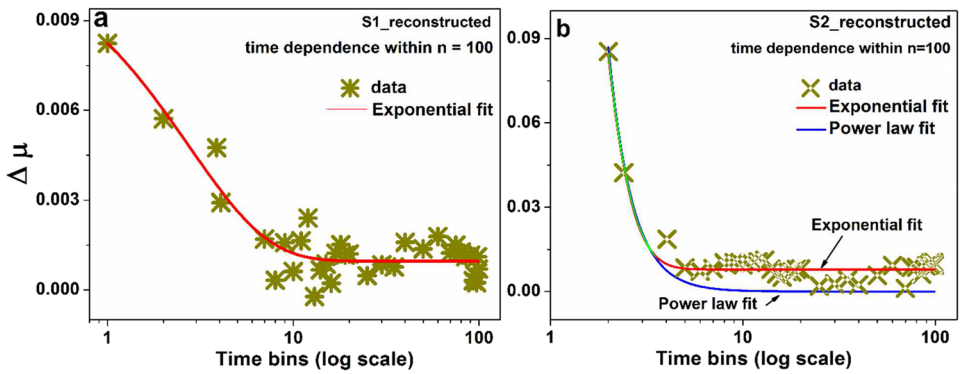

FIG. 7. Dependence of the reconstructed differential XAFS spectra (relative to the corresponding static spectrum) on the number of time bins within a representative pulse. The symbols correspond to the standard deviation values $\Delta\mu$, for both samples S1 (a) and S2 (b), as defined in the text. The two typical exponential and power law relaxation behaviors are shown by fits, where only the exponential fit resulted in reliable goodness of fit parameters ($\chi^2 < 2$).

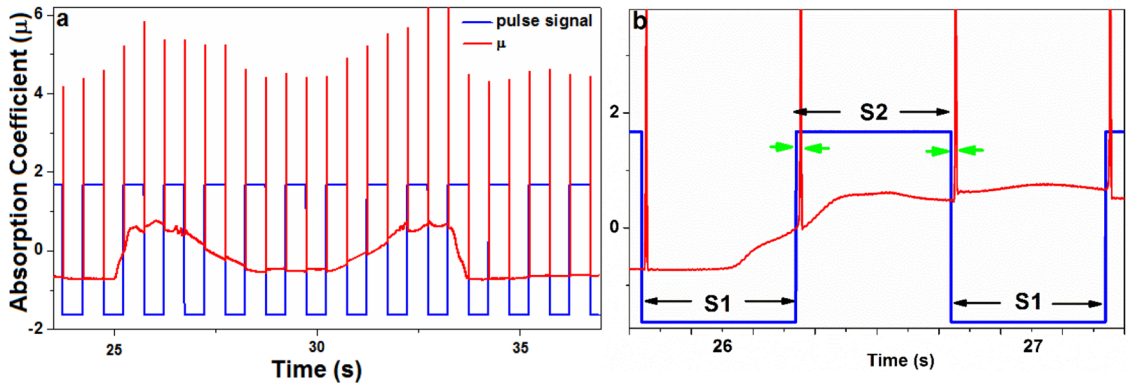

FIG. 8. Raw absorption coefficient data as a function of time and applied pulsed voltage (a). The time lag shown by green arrows (b) originates from the difference between the time the voltage was switched and the sample movement (due to the inductance of the magnetic coil of the actuator).

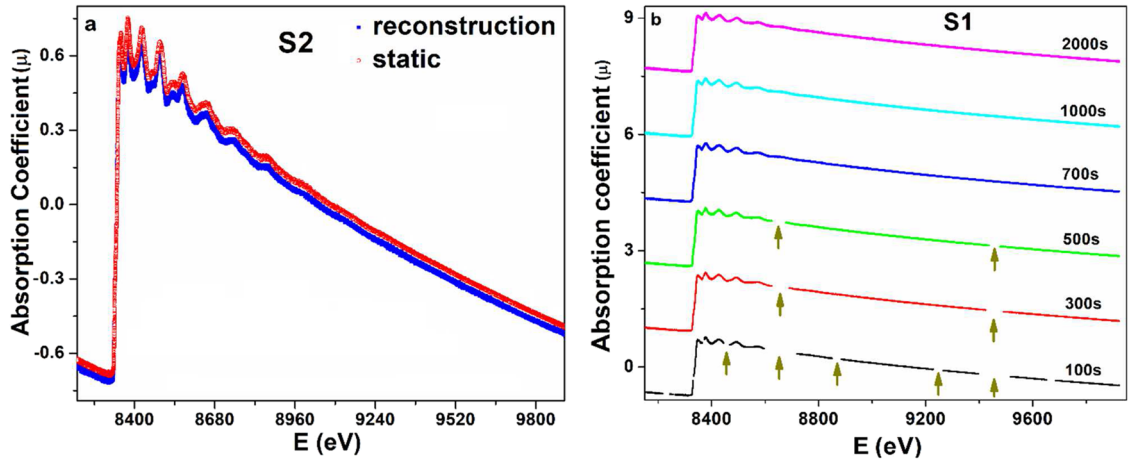

FIG. 9. (a) Reconstruction of the X-ray absorption spectrum in sample S2 for the single pulse interval from the asynchronous data collected during the first 100 s of measurement time. (b) Different reconstruction results for sample S1 obtained for the several measurement times. All spectra correspond to the central part of the pulse divided in 3 time bins. Arrows are marked to guide the eye.

rate and pulse rate used in our case. For example, when X-ray energy scans are faster, the corresponding minimum time for spectral reconstruction will decrease.

C. Quantitative EXAFS data analysis

In Sec. III A, we have demonstrated qualitative agreement between the reconstructed and static XAFS signals. This section investigates quantitatively the level of agreement between the two for the purpose of data analysis and interpretation of realistic modulated systems. To analyze EXAFS data, conventional least-square fitting to the theoretical FEFF6 model, as implemented in the ARTEMIS code,[33] was applied. Data from the Ni K-edge absorption edge was fitted to obtain a structure model, consistent with all available experimental information. Here, we analyze only contributions from the first coordination shell. For these films, the fitted variables were coordination numbers N, corrections to the interatomic distances ΔR, and bond length disorder factors (σ^2) for Ni–Ni and Ni–W pairs. Corrections to photoelectron reference energy ΔE_0 were fitted for each spectrum independently. Amplitude reduction factors $S_0{}^2$ were obtained from the EXAFS data fitting for corresponding Ni metal foil and was set to be equal to 0.69. Theoretical phases and amplitudes were obtained in *ab initio* calculations with the FEFF6 code for bulk materials. The complex exchange-correlation

TABLE III. Structure parameters obtained in the fitting of Ni K-edge EXAFS data.

Sample	$N_{\text{Ni–Ni}}$	$N_{\text{Ni–W}}$	$R_{\text{Ni–Ni}}$ (Å)	$R_{\text{Ni–W}}$ (Å)	$\sigma^2_{\text{Ni–Ni}}$ (Å^2)	$\sigma^2_{\text{Ni–W}}$ (Å^2)	$\Delta E_{0(\text{Ni})}$ (eV)
$S1_{\text{static}}$	8.9(8)	3.2(7)	2.480(6)	2.535(4)	0.010(3)	0.012(1)	−6.0(3)
$S1_{\text{reconstructed}}$	8.8(8)	3.3(9)	2.483(4)	2.53(2)	0.010(1)	0.013(1)	−5.9(4)
$S2_{\text{static}}$	9.9(8)	4.3(7)	2.533(3)	2.552(7)	0.006(1)	0.006(1)	−5.2(3)
$S2_{\text{reconstructed}}$	10.1(6)	4.4(7)	2.534(3)	2.545(3)	0.006(1)	0.007(1)	−5.2(4)

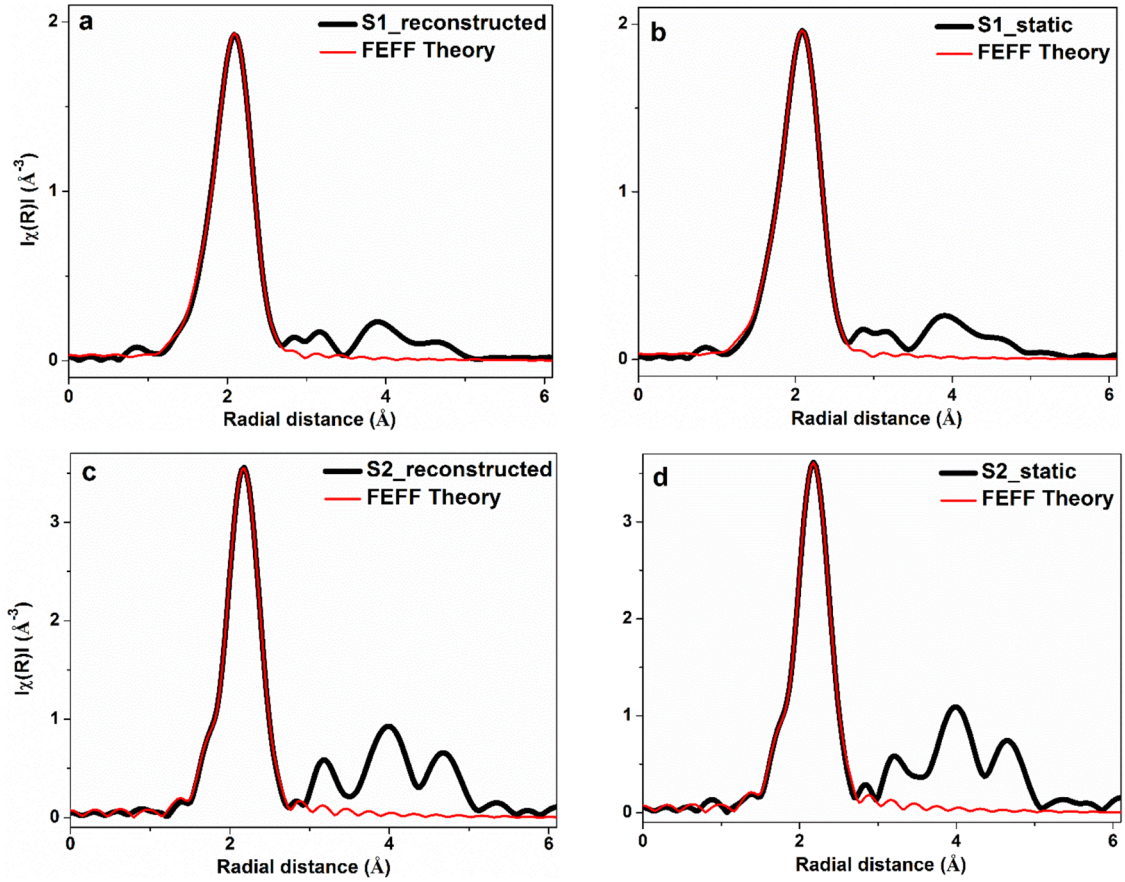

FIG. 10. Fits of Ni K-edge EXAFS for NiW films for the static and the reconstructed S1 [(a) and (b)] and S2 [(c) and (d)] samples.

Hedin-Lundqvist potential and default values of muffin-tin radii as provided within the FEFF6 code were employed. Data fitting was carried out in the range from R_{min} = 1.46 Å up to R_{max} = 2.46 Å. Fourier transform was carried out in the k range from 2.0 Å^{-1} up to 14.0 Å^{-1}. The obtained results are summarized in Table III and Fig. 10. Excellent agreement between the results obtained for the static and reconstructed spectra attests to the validity of our approach, the setup, the sorting algorithm, and the software that implements the data processing and analysis.

IV. CONCLUSION

We reported a new setup for the modulation excitation spectroscopy method at the ISS beamline of NSLS-II. Coupled with high flux and dedicated data acquisition software that enables synchronization of the external stimulation and X-ray spectra, the setup enables a broad range of experiments with periodic external stimulation, aimed at investigation of functional materials with weak structural and electronic responses. Our setup was demonstrated using a test case of two samples with high spectral contrast, which we used to obtain reconstructed spectra corresponding to each spectrum following the completion of the experiment. We have also investigated measurement regimes in terms of the reconstructed signal quality (spectral density and signal to noise ratio), in order to provide guidance to future applications of this setup. The method can be applied to a broad range of problems, from studying novel electromechanical properties in thin films to nanoscale catalysts to battery and solar cell materials.

ACKNOWLEDGMENTS

The research leading to these results received funding through the NSF-BSF program. H.S. and A.I.F. acknowledge support by NSF Grant No. DMR-1701747. I.L. acknowledges the BSF Program Grant No. 2015679. J.R.T. acknowledges support from the NSF CAREER Program under Award No. CMMI-1554411. This research used 8-ID (ISS) beamline of the National Synchrotron Light Source, a U.S. Department of Energy (DOE) Office of Science User Facility operated for the DOE Office of Science by Brookhaven National Laboratory under Contract No. DE-AC02-98CH10886. J.R.T. acknowledges the use of characterization resources in the Center for Functional Nanomaterials, Brookhaven National Laboratory, which is supported by the U.S. Department of Energy, Office of Basic Energy Sciences under Contract No. DE-SC0012704.

[1]M. Newton, Catalysts **7**, 58–107 (2017).
[2]A. I. Frenkel, J. A. Rodriguez, and J. G. Chen, ACS Catal. **2**, 2269–2280 (2012).
[3]R. Korobko, A. Patlolla, A. Kossoy, E. Wachtel, H. L. Tuller, A. I. Frenkel, and I. Lubomirsky, Adv. Mater. **24**, 5857–5861 (2012).
[4]A. D. Ushakov, E. Mishuk, E. Makagon, D. O. Alikin, A. A. Esin, I. S. Baturin, A. Tselev, V. Y. Shur, I. Lubomirsky, and A. L. Kholkin, Appl. Phys. Lett. **110**, 142902–142904 (2017).

[5]K. W. Chapman, MRS Bull. **41**, 231–240 (2016).
[6]M. Giorgetti, ISRN Mater. Sci. **2013**, 1–22.
[7]P. Müller and I. Hermans, Ind. Eng. Chem. Res. **56**, 1123–1136 (2017).
[8]T. M. Usher, J. E. Daniels, and J. L. Jones, Sci. Rep. **5**, 14678–14688 (2015).
[9]R. F. Pettifer, S. Pascarelli, M. D. Cooke, and M. R. J. Gibbs, Nature **435**, 78–81 (2005).
[10]R. Korobko, A. Lerner, Y. Li, E. Wachtel, A. I. Frenkel, and I. Lubomirsky, Appl. Phys. Lett. **106**, 042904–042905 (2015).
[11]A. I. Frenkel, A. Yevick, C. Cooper, and R. Vasic, Annu. Rev. Anal. Chem. **4**, 23–39 (2011).
[12]M. P. Ruffoni, S. Pascarelli, R. Grossinger, R. S. Turtelli, C. Bormio-Nunes, and R. F. Pettifer, Phys. Rev. Lett. **101**, 147202–147204 (2008).
[13]D. Ferri, R. Wirz, A. Eyssler, O. Korsak, P. Hug, A. Weidenkaff, and M. A. Newton, Phys. Chem. Chem. Phys. **12**, 5634–5646 (2010).
[14]C. F. J. König, J. A. van Bokhoven, T. J. Schildhauer, and M. Nachtegaal, J. Phys. Chem. C **116**, 19857–19866 (2012).
[15]D. Baurecht and U. P. Fringeli, Rev. Sci. Instrum. **72**, 3782–3792 (2001).
[16]A. Urakawa, T. Bürgi, and A. Baiker, Chem. Eng. Sci. **63**, 4902–4909 (2008).
[17]A. Urakawa, T. Bürgi, and A. Baiker, Chem. Phys. **324**, 653–658 (2006).
[18]C. F. J. König, T. J. Schildhauer, and M. Nachtegaal, J. Catal. **305**, 92–100 (2013).
[19]G. L. Chiarello and D. Ferri, Phys. Chem. Chem. Phys. **17**, 10579–10591 (2015).
[20]D. Ferri, M. A. Newton, and M. Nachtegaal, Top. Catal. **54**, 1070–1078 (2011).
[21]J. Szlachetko, D. Ferri, V. Marchionni, A. Kambolis, O. V. Safonova, C. J. Milne, O. Krocher, M. Nachtegaal, and J. Sa, J. Am. Chem. Soc. **135**, 19071–19074 (2013).
[22]M. A. Newton, C. Belver-Coldeira, A. Martinez-Arias, and M. Fernandez-Garcia, Nat. Mater. **6**, 528–532 (2007).
[23]A. Kossoy, A. I. Frenkel, Q. Wang, E. Wachtel, and I. Lubomirsky, Adv. Mater. **22**, 1659–1662 (2010).
[24]Y. Li, O. Kraynis, J. Kas, T. C. Weng, D. Sokaras, R. Zacharowicz, I. Lubomirsky, and A. I. Frenkel, AIP Adv. **6**, 055320–055327 (2016).
[25]K. Okamoto, K. Okamoto, K. Kohdate, K. Nagai, J. Miyawaki, H. Kondoh, T. Yokoyama, A. Nojima, and T. Ohta, Int. Union Crystallogr. **10**, 242–247 (2003).
[26]M. P. Ruffoni, J. Synchrotron Radiat. **16**, 591–594 (2009).
[27]G. M. Wang, T. Shaftan, W. X. Cheng, W. Guo, P. Ilinsky, Y. Li, B. Podobedov, and F. Willeke, Rev. Sci. Instrum. **87**, 033301 (2016).
[28]R. Kadyrov, K. Ha, E. Stavitski, J. De Long, and S. L. So, in *Proceedings of ICALEPCS, Melbourne, Australia* (CERN, 2015), pp. 881–884, WEPGF080.
[29]B. V. Luvizotto, K. Attenkofer, E. Stavitski, and H. Bassan, in *Proceedings of ICALEPCS, Barcelona, Spain* (Geneva, 2017), pp. 962–965, TUPHA211.
[30]A. J. Dent, P. C. Stephenson, and G. N. Greaves, Rev. Sci. Instrum. **63**, 856–858 (1992).
[31]A. K. Jonscher, Nature **267**, 673–679 (1977).
[32]A. K. Jonscher, J. Phys. D: Appl. Phys. **32**, 57–70 (1999).
[33]B. Ravel and M. Newville, J. Synchrotron Radiat. **12**, 537–541 (2005).